

Polymer–Doxorubicin Conjugate Micelles Based on Poly(ethylene glycol) and Poly(*N*-(2-hydroxypropyl) methacrylamide): Effect of Negative Charge and Molecular Weight on Biodistribution and Blood Clearance

Qingsong Yu,^{†,‡} Zhenke Wei,^{†,§} Jiyun Shi,^{||} Shuli Guan,[‡] Nan Du,[‡] Tong Shen,[‡] Hao Tang,[‡] Bing Jia,^{||} Fan Wang,^{||} and Zhihua Gan^{*,‡,§}

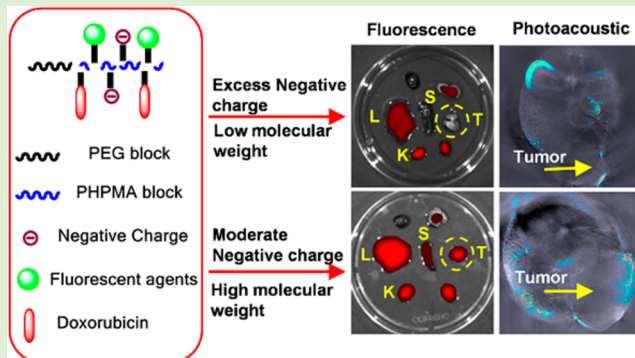
[†]The State Key laboratory of Organic–inorganic Composites, Beijing Laboratory of Biomedical Materials, College of Life Science and Technology, Beijing University of Chemical Technology, Beijing 100029, China

[§]The CAS Key Laboratory of Engineering Plastics, Institute of Chemistry, Chinese Academy of Sciences (CAS), Beijing 100190, China

^{||}Medical Isotopes Research Center, Peking University, Beijing 100191, China

Supporting Information

ABSTRACT: Well-defined water-soluble block copolymers poly(ethylene glycol)-*b*-poly(*N*-(2-hydroxypropyl) methacrylamide-*co*-*N*-methacryloylglycylglycine) (PEG-*b*-P(HPMA-*co*-MAGG)) and their doxorubicin (Dox) conjugates with different composition and molecular weight were synthesized. These Dox conjugates can form micelles in buffer solution. The physicochemical properties, in vivo biodistribution, blood clearance, and especially the tumor accumulation of copolymers and micelles were studied. Severe liver accumulation can be observed for PEG-*b*-PMAGG copolymers. This was quite different from their Dox conjugate for which decreased RES uptake and elevated kidney accumulation could be observed. When decrease the negative charge to an appropriate amount such as 8–10 mol %, both RES uptake and kidney accumulation could be suppressed. Obvious tumor accumulation could be achieved especially when the molecular weight were increased from ~40 to ~80 KDa. These results provided us with a guideline for the design of nanoscaled drug delivery system as well as a potential option for treating kidney-related cancers.



1. INTRODUCTION

Over the past decades, polymer therapeutics have been intensively studied for anticancer drug delivery regarding their potential to change the body distribution of drugs.^{1,2} The key benefits of these drug delivery systems compared to the low molecular weight anticancer drugs are the increase of plasma half-life and reduction of toxic side effects, as well as the enhanced tumor accumulation,^{3,4} due to the enhanced permeation and retention (EPR) effect.^{5–7}

The basic requirements for polymers as drug carriers are nontoxic, nonimmunogenic, and can be eliminated by the body. Among those polymer drug delivery systems, the water-soluble drug conjugates based on poly(ethylene glycol) (PEG)^{8,9} and *N*-(2-hydroxypropyl) methacrylamide (HPMA) copolymers^{10–12} rank the most intensively studied. PEGylation is an efficient way to enhance the pharmacokinetic properties of anticancer drugs.⁸ Due to its “stealth” property, PEG minimize the identification by the opsonin protein and thus reduce the uptake by the reticuloendothelial system (RES).¹³ However, the lack of functional group makes its application greatly

restricted. In this regard, HPMA copolymers hold the most favorable characteristics. Besides its nontoxic, nonimmunogenic, and biocompatible properties, its potential application has also been proved by diverse experimental or clinical studies.^{14,15} A variety of methods have been explored to improve the tumor accumulation of active agents while reducing their systemic toxicity.¹⁶ Even though the tumor targeting potential can be retained effectively after introduction of functional groups. The pharmacokinetics, the tissue distribution, and the tumor accumulation of PHPMA copolymers will be influenced and the absolute levels in blood and tumor decrease after the modification.¹⁷ How to introduce functional groups while maintaining carrier pharmacokinetic properties is still a major concern. The introduction of PEG into PHPMA drug conjugates have been proved to efficiently improve the biodistribution and pharmacokinetic

Received: April 8, 2015

Revised: June 11, 2015

Published: July 2, 2015

characteristics in living animal. For instance, Allmeroth and co-workers have reported that the grafted PEG in poly(*N*-(2-hydroxypropyl)methacrylamide)-*block*-poly(lauryl methacrylate) (PHPMA-*b*-PLMA) copolymers lead to a smaller size for the nanoaggregates thus bring more optimal body distribution pattern and higher blood pool concentration. Besides, compared with the pure PHPMA-*b*-PLMA copolymers, a continuous increase of tumor accumulation could be found with the increase of PEGylation degree for the PEGylated copolymers.¹⁸ Wang and co-workers report that the introduction of PEG and PHPMA into the dextran graft copolymers can increase the blood pool concentration of dextran graft poly(*N*-methacryloylglycylglycine)-tyrosine conjugates (Dex-*g*-PMAGGCONHTyr).¹⁹

Previous systematical studies in our group have already revealed that not only the PEG block but also the net charge of the poly(ethylene glycol)-*b*-poly[(*N*-(2-hydroxypropyl) methacrylamide)-*co*-(*N*-methacryloylglycylglycine)] (PEG-*b*-P-(HPMA-*co*-MAGG)) copolymers possessed major impact on the body distribution and pharmacokinetics. Longer PEG block length and slight negative charge is beneficial for prolonging the plasma half-life and optimal biodistribution pattern.²⁰ However, those studies are carried out under the circumstances without any payload and tumor bearing mice. In addition, we believe that the polymer–drug conjugates may change the solution behavior accordingly after the polymers conjugate anticancer drugs. Therefore, more detailed investigations on the impact of negative charge and drug-conjugation of polymers need to be accomplished.

Recently, in order to characterize the biodistribution of drug delivery systems noninvasively, lots of imaging techniques such as single-photon emission computed tomography (SPECT), positron emission tomography (PET),²¹ gamma scintigraphy, and macroscopic near-infrared fluorescence (NIRF) imaging^{22,23} as well as photoacoustic (PA) imaging^{24,25} have been developed. These techniques allow visualization of the target signals *in vivo* quantitatively, in real-time or with high spatial resolution, which enable the noninvasive study of pharmacokinetics and biodistribution.²⁶

Herein, to investigate the impact of negative charge and PEG block of the polymer-drug conjugate on their biodistribution and pharmacokinetic behaviors, a series of linear PEG-*b*-P(HPMA-*co*-MAGG) block copolymers were synthesized by RAFT polymerization. Anticancer drug, doxorubicin (Dox), was conjugated to the polymer backbone via an acid-labile hydrazone bond. The radioactive nuclide iodine (¹²⁵I) and near-infrared (NIR) fluorescent dye Cy7 were introduced by tyrosine residue and azide group on the main chain, respectively. Besides *ex vivo* biodistribution, the *in vivo* biodistribution and blood clearance of polymers and polymer–drug conjugate micelles with a different amount of negative charge and molecular weight were investigated by gamma imaging, NIR fluorescent imaging, and photoacoustic imaging techniques.

2. EXPERIMENTAL METHODS

2.1. Materials. *N*-(2-Hydroxypropyl)methacrylamide (HPMA, reagent grade, Polysciences Inc.), 4,4'-azobis(cyanopentanoic acid) (V501, >98%, Fluka), tyrosine (Tyr, >98%, Alfa Aesar), 4-(*N,N*-dimethylamino)pyridine (DMAP, 99%, Alfa Aesar), propargylamine, Iodogen (Sigma, Shanghai, China), Na¹²⁵I (Beijing Atom High Tech, Beijing, China), PD MiniTrap column (GE Healthcare, Buckingmashe, U.K.), and Cy7-NHS (Lumiprobe, Hallandale Beach, FL) were

used as received without further purification. Water (HPLC grade) was obtained with a Milli-Q system (Millipore, Bedford, MA). Sodium cholate was purchased from Sigma Chemical Co. Dichloromethane and acetonitrile (PA grade) were obtained from Acros Organics. The ITLC method used Gelman Sciences silica-gel paper strips and acetone as eluent. The other chemicals (reagent grade) in this work were purchased from Aldrich and used without purification. 4-Cyanopentanoic acid dithiobenzoate (CPAD),²⁷ PEG macro chain transfer agent (PEG-CTA),²⁸ *N*-methacryloylglycylglycine (MAGG),²⁹ *N*-(*tert*-butoxycarbonyl)-*N'*-(methacryloylglycylglycyl) hydrazine (BHMAGG),³⁰ methacryloyl tyrosyl methyl ester (MA-Tyr),²⁰ and *N*-(3-azidopropyl) methacrylamide (AzMA)³¹ were synthesized according to the literature procedure.

2.2. Synthesis and Radiolabeling of PEG-*b*-PMAGG-Tyr Diblock Copolymers. The PEG-*b*-PMAGG-Tyr copolymers were synthesized according to our previously reported procedure.²⁰ Briefly, for PEG_{5k}-*b*-PMAGG_{40k}, an aqueous solution of PEG-CTA (1.30 g, 0.25 mmol), MAGG (10.4 g, 50 mmol), MA-Tyr (0.32 g, 1 mmol), and V501 (35 mg, 0.125 mmol) in DMSO was added in a glass tube. After degassed in liquid nitrogen and filled with argon, the tube was sealed and the polymerization was conducted at 70 °C for a given time. The polymerization was halted by immersing into liquid nitrogen immediately. The product was isolated by dialysis in distilled water at room temperature and then followed by lyophilization. The PEG-*b*-PMAGG block copolymer was obtained as pink powder.

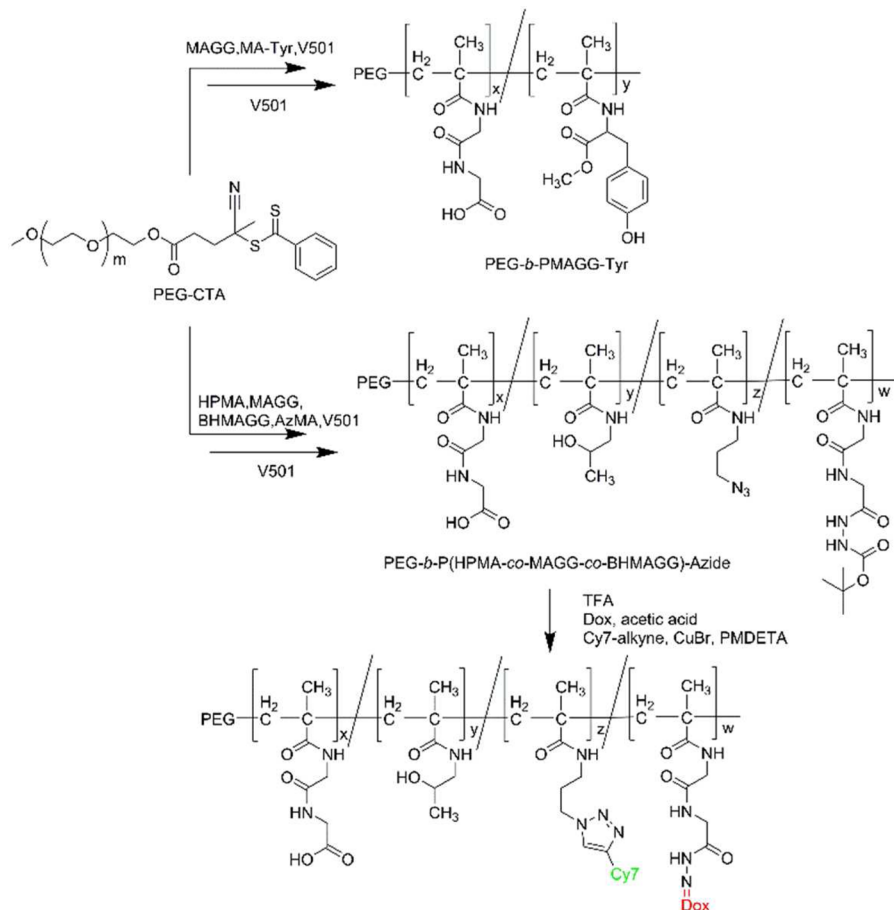
The labeling of radio isotope ¹²⁵I was carried out according to literature reported procedure. All ¹²⁵I radiotracers were purified using PD MiniTrap column before animal studies. The PD MiniTrap column was washed with 6 mL of PBS and activated with 2 mL of 1% BSA before purification. After the PD MiniTrap column was loaded with radiotracer (~100 μ L), it was washed with 4 mL of PBS and the eluent between 0.6 and 1.1 mL was collected. The purity and stability of radiolabeled polymer were monitored by instant thin layer chromatography (ITLC). Doses for animal studies were prepared by dissolving the purified radiotracer in saline to give a concentration of 100 μ Ci/mL for biodistribution studies and 2.5 mCi/mL for scintigraphic imaging. Each mouse was injected with 0.1 mL of radiotracer solution.

2.3. Synthesis of PEG-*b*-P(HPMA-*co*-MAGG-*co*-BHMAGG)-Azide, Conjugation of Dox, and Labeling of NIR Fluorescent Dye. PEG-*b*-P(HPMA-*co*-MAGG-*co*-BHMAGG)-azide copolymers and their Dox conjugates were prepared according to our previously reported procedure, except for the addition of AzMA.³⁰ The labeling process of NIR dye Cy7 was accomplished by a two-step reaction. First, Cy7-NHS (5 mg) was reacted with 3-fold excess of propargylamine in the presence of trimethylamine in anhydrous DMSO. The crude product Cy7-alkyne was obtained by precipitation in diethyl ether and used without further purification. Second, a 3-fold excess of Cy7-alkyne relative to the azide group was reacted with PEG-*b*-P(HPMA-*co*-MAGG-*co*-BHMAGG)-azide copolymers in the presence of equal molar copper sulfate, ascorbic acid, and PMDETA via “click chemistry”.

2.4. Characterization of Polymer Precursors and Polymer Conjugates. **2.4.1. Molecular Weight and Hydrodynamic Size.** The molecular weight was determined using size-exclusion chromatography with multiangle laser light scattering and refractive index detection (SEC-MALLS-RI). The chromatographic system consisted of a 1500 Alliance HPLC equipped with a manual sampler (Wyatt Technologies, Santa Barbara, CA). The injector was fitted with a 50 μ L injection loop. All separations were performed using a mobile phase of 0.1 M sodium nitrate in 0.02% sodium azide or 0.05 M lithium bromide in *N,N*-dimethylformamide at a flow rate of 1.0 mL/min. Both the MALLS detector and RI detector (DAWN HELEOS-II and OptiLab rEX, Wyatt Technologies, Santa Barbara, CA) used a 690 nm laser. Elution diagrams were analyzed by using the ASTRA 4.73.04 software from Wyatt Technology. The chemical structure of the copolymers was analyzed by Bruker AVANCE 400 MHz ¹H NMR.

The size of all copolymer and corresponding polymer conjugates in water was determined using a Zeta-Sizer (Zeta-Sizer Nano Series; Malvern, Worcestershire, U.K.).

Scheme 1. Synthetic Routes of PEG-*b*-PMAGG-Tyr (P5Mx), PEG-*b*-P(HPMA-*co*-MAGG-*co*-BHMAGG)-Azide Copolymers (P5(HyMz)*m*B), and Their Conjugates with Dox and Cy7 (P5(HyMz)*m*-D) via RAFT Polymerization and Post-Polymerization Modification Technique



2.4.2. Content of Cy7 in Polymer Conjugates. The content of Cy7 in the conjugates were determined by quantitative UV spectrophotometry of polymer solutions in PBS buffer (pH = 7.4) using an UV-vis spectrophotometer (Shimadzu UV 2450).

2.4.3. Dox and Tyrosyl Residue Content. The content of covalently conjugated Dox was determined by ¹H NMR spectra on a Bruker AVANCE (400 MHz) spectrometer using TMS as internal standard and DMSO-*d*₆ as solvent.

2.4.4. Fluorescence Spectra. The fluorescence spectra (770–900 nm) of polymer conjugates containing Cy7 were recorded with an excitation at 750 nm using a Cary eclipse fluorescence spectrophotometer (Varian, Darmstadt, Germany).

2.4.5. Cell Culture. The BALB/c mouse breast cancer cell line (4T1) were grown in RPMI 1640 medium supplemented with 10% (v/v) fetal bovine serum (FBS), 1% (v/v) penicillin–streptomycin antibiotics, and 2 mM L-glutamine. Cells were maintained at 37 °C in a humidified atmosphere of 5% carbon dioxide and 95% air.

2.4.6. Animals. Five-week-old female BALB/c mice were used in compliance with the Institutional Animal Care and Use Committee of Peking University. The mice were fasted for a brief period before the experiment to allow comparable results. During the experiment the animals were under either sodium pentobarbital (45.0 mg/kg) or isoflurane anesthesia (1.8% at 0.8 L/min).

2.5. Pharmacokinetics of PEG-*b*-PMAGG in Normal Mice. Seven BALB/c mice were used as one group for the blood clearance experiment of one compound. The ¹²⁵I-radiotracer (10 μCi in 0.1 mL of saline) was administered intravenously to each mouse. Animals were sacrificed by cervical dislocation after being anesthetized with an intraperitoneal injection of sodium pentobarbital at a dose of 45.0 mg/kg at 1, 3, 5, 7, 10, 15, 20, 30, 60, 90, and 120 min post-injection (p.i.).

Blood was harvested and weighed; the radioactivity was measured in a γ -counter (Wallac 1470–002, PerkinElmer, Finland). The plasma concentration was calculated as a percentage of the injected dose per gram of wet tissue mass (%ID/g).

2.6. Biodistribution of PEG-*b*-PMAGG in Normal Mice. Sixteen BALB/c mice were randomly divided into four groups, each of which had four animals. The ¹²⁵I-radiotracer (10 μCi in 0.1 mL saline) was administered intravenously to each mouse. Animals were sacrificed by cervical dislocation at 1, 4, 24, and 48 h p.i. Blood, brain, heart, liver, spleen, kidney, stomach, muscle, bone, large intestine, small intestine, and feces were harvested, weighed, and measured for radioactivity in a γ -counter (Wallac 1470–002, PerkinElmer, Finland). The organ uptake was calculated as both a percentage of injected dose per organ (%ID/organ) and a percentage of injected dose per gram of wet tissue mass (%ID/gram).

The biodistribution data and blood clearance curve are reported as an average plus the standard variation. Comparison between two different radiotracers was also made using the one-way ANOVA test (Graph Pad Prism 5.0, San Diego, CA). The level of significance was set at *p* = 0.05.

2.7. Scintigraphic Imaging in 4T1 Tumor Bearing Mice. The imaging study was performed using three 4T1 tumor bearing female BALB/c mice. Before imaging, each BALB/c mouse was subcutaneously injected 1×10^6 4T1 cells. When the tumor size reached 100 mm³, each animal was administered with 500 μCi of ¹²⁵I labeled copolymers in 0.2 mL of saline. Animals were then anesthetized with intraperitoneal injection of sodium pentobarbital at a dose of 45.0 mg/kg, then were placed supine on a three-head γ -camera (GE Healthcare, Millennium VG SPECT) equipped with a parallel-hole, low energy, and high-resolution collimator. Anterior images were acquired at 0.5,

1, 2, 4, and 24 h post-injection and stored digitally in a 128×128 matrix. The acquisition count limits were set at 200 K. After completion of the imaging study, animals were sacrificed by cervical dislocation.

2.8. In Vivo Optical Imaging of Micelles in 4T1 Tumor Bearing Mice. The imaging study was performed using three 4T1 tumor bearing female BALB/c mice. The mice were anesthetized by isoflurane and placed supine on the imaging stage. Optical imaging of the polymer–Dox conjugate in tumor bearing mice was conducted on an IVIS Spectrum in vivo imaging system (PerkinElmer, U.S.A) using 745/800 filter combination. The photo was acquired and analyzed by Living Image version 4.4 In Vivo Imaging Software (PerkinElmer, U.S.A), and the exposure time, F/stop, and Binning values were set as 1 s, 1 and 4 for all pictures. The images were intensity weighted and displayed using the hot color profile.

2.9. In Vivo Photoacoustic Imaging of the Micelles in 4T1 Tumor Bearing Mice. All phantom and in vivo imaging experiments were performed according to the literature reported procedure^{32,33} using a real-time multispectral optoacoustic tomographic (MSOT) imaging system; inVision 256 (iThera Medical GmbH, Neuherberg, Germany). Optical excitation was provided by an optical parametric oscillator (OPO) with a tunable NIR wavelength range from 680 to 980 nm. PA signals were acquired using a 256-element concave transducer array spanning a circular arc of 270° with a frame rate of 10 Hz. Ultrasound gel was applied on the mouse skin surface, and measurements were recorded in temperature-controlled water for good acoustic coupling. An animal holder with a thin polyethylene membrane was used to prevent direct contact between the mouse and the water.

3. RESULTS AND DISCUSSION

3.1. Synthesis and Characterization of Copolymers and Polymer Conjugates. Scheme 1 shows the synthetic routes of PEG-*b*-PMAGG and PEG-*b*-P(HPMA-*co*-MAGG) block copolymers and their relevant conjugates. As a supplement to our previous work, PEG-*b*-PMAGG-Tyr copolymers with different MAGG content and tyrosyl residue for radioactive iodine (^{125}I) labeling were synthesized to unveil whether the MAGG content have influence on the blood clearance and biodistribution of electronegative PEG-*b*-PMAGG copolymers. The PEG-*b*-P(HPMA-*co*-MAGG-*co*-BHMAAGG)-Azide copolymers containing BHMAAGG and AzMA were synthesized to characterize the impact of negative charge and molecular weight on the blood clearance and biodistribution of drug-loaded copolymers. Anticancer drug Dox was attached to the copolymer via an acid-labile hydrazone bond that showed pH-responsive drug release properties (data not show). To avoid the undesired decomposition or side reactions of conjugated drug in the process of iodine labeling, the NIR fluorescent dye Cy7 was introduced for in vivo imaging study via AzMA by “click chemistry” under relatively mild conditions. The chemical structure and molecular weight of as-prepared copolymers were confirmed by ^1H NMR and SEC, respectively. The amount of Cy7 was determined photometrically in DMSO. The amount of tyrosyl residue and loaded drug were determined by ^1H NMR. For the ease of nomenclature, PEG-*b*-PMAGG-Tyr copolymers were abbreviated as PSM x in which x stands for the theoretical molecular weight of PMAGG block. PEG-*b*-P(HPMA-*co*-MAGG-*co*-BHMAAGG-*co*-AzMA)-Dox-Cy7 conjugates were abbreviated as P5(HyMz) m -D in which y and z represent the molar ratio of HPMA in MAGG in the block, and m represents the theoretical molecular weight of the block. The PEG-*b*-P(HPMA-*co*-MAGG-*co*-BHMAAGG-*co*-AzMA) copolymers before conjugation of Dox and Cy7 were abbreviated as P5(HyMz) m B. In all

above acronyms, P, H, M, B, and D stand for PEG, HPMA, MAGG, BHMAAGG, and Dox, respectively.

Table 1 summarizes the characterization of all copolymers. Narrow molecular weight distribution and molecular weight

Table 1. Characterization of PEG-*b*-PMAGG-Tyr and PEG-*b*-P(HPMA-*co*-MAGG-*co*-BHMAAGG)-Azide Copolymers

sample name	H% ^a	M% ^a	B% ^a	Tyr% ^a	M_w ^a	PDI ^b
PSM20	0	0	0	4.0	25300	1.10
PSM40	0	100	0	4.2	44600	1.11
PSM60	0	100	0	4.1	69500	1.13
PSM80	0	100	0	4.9	83600	1.06
H25B	90.6	0	9.4	0	30400	1.12
PSH20B	91.8	0	8.2	0	30100	1.08
PSM20B	0	88.5	11.5	0	29500	1.13
P5(H8M1)20B	82.1	10.9	9	0	28800	1.11
P5(H8M1)80B	80.3	10.5	9.2	0	84800	1.09

^aH%, M%, B%, and Tyr% represents the molar percentage of HPMA, MAGG, BHMAAGG, and tyrosyl residue in P(HPMA-*co*-MAGG) block of the copolymers, respectively. M_w represents molecular weight of P(HPMA-*co*-MAGG) block in the final polymers. All of the above data were calculated from ^1H NMR in DMSO-*d*₆. ^bThe polydispersity index was determined by SEC in DMF with 50 mM lithium bromide.

adjacent to predetermined value could be observed in this table. This indicated that the RAFT polymerization of HPMA, MAGG, BHMAAGG, and AzMA via PEG_{5k}-CTA was a controllable process which guarantees the study of the precise structure–property correlation.

Figure 1 shows the representative ^1H NMR spectra, UV–vis absorption spectra, and size distribution of micelles. The rest ^1H NMR spectra could be found in the Supporting Information (Figure S1). In order to characterize the size and size distribution of polymer–Dox conjugates, we measured the UV–vis adsorption spectra of polymer–Dox conjugates without Cy7. It can be found that, at the laser wavelength of the DLS instrument (~ 633 nm), the conjugates show almost no adsorption; thus, the interference of fluorescence and adsorption could be eliminated. From the NMR spectra of P5(H8M1)20-D we can find out that the characteristic signals of Dox disappeared in water. On the other hand, these conjugates show sizes around 10 nm. These results indicated that micelle-like aggregation forms in water for all polymer–Dox conjugates with partially hydrophobic Dox flipped inside the micelle core. The comparison between the size of H25-D and P5(H8M1)20-D showed no significant difference, indicating that the introduction of 5 kDa PEG does not significantly affect the hydrodynamic size of the conjugates. The drug loading parameters such as drug loading content (DLC) and drug loading efficiency (DLE) could be found in Table S1. The high DLC and DLE value together shows the advantage of polymer–drug conjugate compared with other drug delivery systems in which the drugs are physically entrapped.

Table 2 shows the solution properties of PSM x copolymers and P5(HyMz) m -D conjugates. The molar percentage of tyrosine or Cy7 were maintained to be around 5% for PSM x copolymers and P5(HyMz) m -D conjugates, respectively. In order to investigate the influence of composition and negative charge, the molecular weight of PSH20-D, PSM20-D, and P5(H8M1)20-D were set below the renal threshold to minimize the retention caused by large molecular weight.

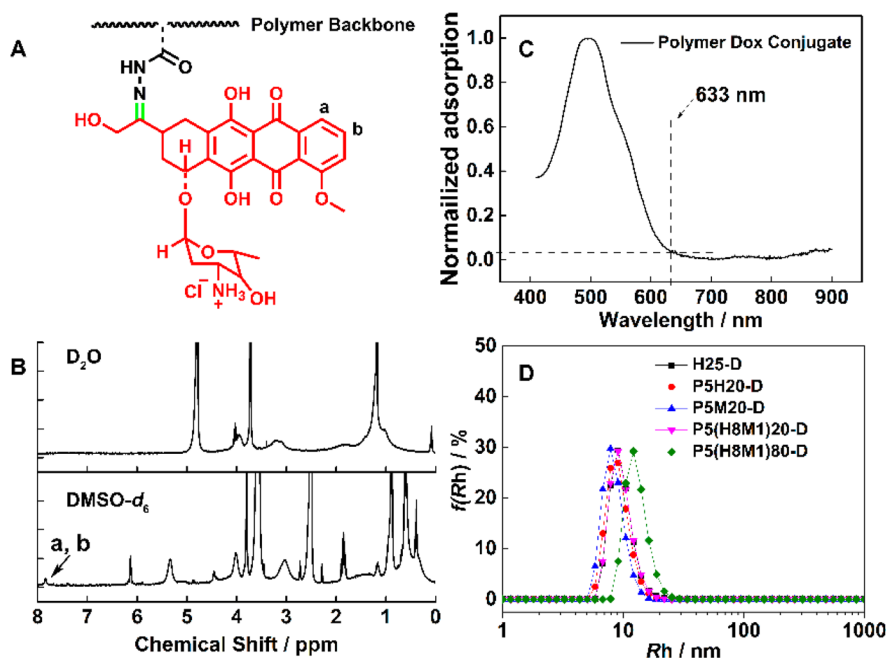


Figure 1. (A) Chemical structure of polymer conjugated Dox. (B) ¹H NMR spectra of polymer–Dox conjugate P5(H8M1)20-D in ¹D₂O and ¹DMSO-d₆. (C) UV–vis absorption spectra of polymer–Dox conjugates P5(H8M1)20-D without Cy7. (D) Size distribution by number of H20-D, PSH20-D, PSM20-D, P5(H8M1)20-D, and P5(H8M1)80-D micelles in 10 mM PBS.

Table 2. Physicochemical Properties of PEG-*b*-PMAGG-Tyr and PEG-*b*-P(HPMA-*co*-MAGG-*co*-HMAGG-*co*-AzMA)-Dox-Cy7 Conjugate Micelles

sample name	D% ^a	Cy7% ^b	R _h ^c (nm)	zeta potential ^e (mV)
PSM20	0	0	4.38 ± 0.63	-33.5 ± 6.3
PSM40	0	0	5.36 ± 1.15	-36.9 ± 7.2
PSM60	0	0	6.69 ± 0.77	-39.4 ± 5.5
PSM80	0	0	7.51 ± 1.08	-45.7 ± 7.5
H25-D	7.2	0	8.42 ± 1.12	-8.7 ± 3.1
PSH20-D	7.4	4.5	9.20 ± 2.15 ^d	-16.3 ± 6.4 ^d
PSM20-D	6.9	4.6	10.13 ± 1.14 ^d	-30.1 ± 5.4 ^d
P5(H8M1)20-D	7.8	5.1	9.13 ± 1.87 ^d	-20.8 ± 7.2 ^d
P5(H8M1)80-D	8.1	4.3	15.45 ± 2.98 ^d	-15.9 ± 5.1 ^d

^aD% represent the molar percentage of Dox in the final polymer conjugates which was determined by ¹H NMR in DMSO-d₆. ^bCy7% represent the molar percentage of Cy7 in the final polymer conjugates which was determined photometrically from the UV–vis spectra of the polymer conjugates in DMSO. ^cThe hydrodynamic radius and zeta potential of the block copolymers was determined by a Malvern zetasizer in 10 mM phosphate buffer (pH = 7.4). ^dThe size and zeta potential of polymer–Dox conjugates was measured before the conjugation of Cy7 with an instrument equipped a 633 nm laser.

H25-D was synthesized to investigate the influence of the introduction of 5 kDa PEG on the zeta potential of micelles.

As shown in Table 2, the polymer conjugates with higher molecular weight showed larger size than their lower molecular weight counterpart. Compared with the copolymers PSM40, polymer–drug conjugates, such as PSH20-D, PSM20-D, and P5(H8M1)20-D, with similar molecular weights exhibited larger size, which could be attributed to the introduction of the partially hydrophobic anticancer drug. Accordingly, P5(H8M1)80-D with highest molecular weight and highest amount of Dox showed largest hydrodynamic size.

As can be seen from Table 2, all copolymers and micelles showed negative net charge. With the introduction of MAGG, the net charge became more negative. The more the amount of MAGG, the more negative the net charge of micelles. After the conjugation of Dox, the zeta potential values of micelles were higher than the corresponding copolymers. This could also be explained by the partially hydrophobic characteristic of Dox which caused the formation of aggregates. Because Dox and MAGG was in the same block, the inversion of Dox will inevitably take along the approaching MAGG, thus, resulting in the decrease of zeta potential value. From the comparison of the zeta potential of H25-D and PSH20-D, we can conclude that the introduction of PEG make the zeta potential of the conjugates more negative.

In order to quantitatively investigate the pharmacokinetics and biodistribution of PSM_x copolymers while ensuring data comparability with our previous work,²⁰ PSM_x copolymers were labeled with radionuclide ¹²⁵I by the Iodogen method and then subjected to gamma scintigraphic analysis. The solution stability of the resultant radio-labeled copolymers were characterized (Figure S2A,B). The radiochemical purity (RCP) of ¹²⁵I labeled PEG-*b*-PMAGG after PD MiniTrap column purification was higher than 99%. The in vitro stability assay (Figure S2C) showed that the radiolabeled copolymers were stable in PBS buffer for up to 72 h. In order to investigate the blood clearance and biodistribution of polymer–Dox conjugates noninvasively, the P5(HyMz)_m-D conjugates were labeled with NIR fluorescent dye Cy7 and subjected to fluorescent and photoacoustic analysis. As shown in Figure S3A, Cy7-labeled polymer conjugates showed similar absorption spectra to free Cy7, which proved the feasibility of the labeling process. The stability of Cy7 fluorescence of the labeled polymer conjugates was determined by fluorescence spectroscopy after standing in the dark for different time. As shown in Figure S2D, the stable fluorescence guarantees the

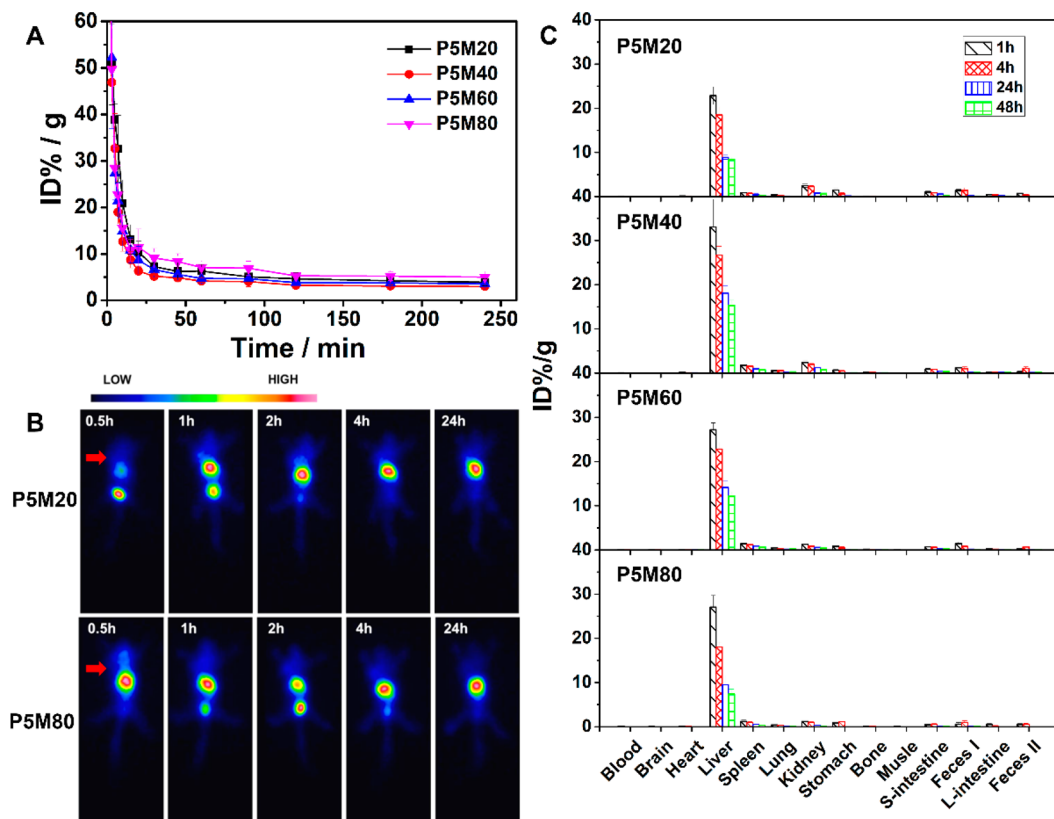


Figure 2. (A) Blood clearance of PEG-*b*-PMAGG in BALB/c normal mice. Each data point represents an average of blood clearance data in seven animals. (B) Scintigraphic analysis of the BALB/c mice bearing 4T1 tumor administered with $\sim 500 \mu\text{Ci}$ of radiotracer P5M20 and P5M80. Tumour is marked with red arrow. (C) Histograms of biodistribution data for PEG-*b*-PMAGG copolymers at different times in normal BALB/c mice. The organ uptake was calculated as a percentage of injected dose per gram of wet tissue (%ID/g). Each data point represents an average of biodistribution data in four animals. a, b, c, and d denote the copolymers with PMAGG block molecular weight as 20k, 40k, 60k, and 80k, respectively.

long-term study of the pharmacokinetic behavior of the conjugates for up to 72 h.

To discriminate the injected chromophores from the intrinsic absorbers such as oxy- and deoxyhemoglobin (HbO_2 and Hb), the spectral signatures of Hb , HbO_2 , and Cy7 between 680–900 nm were imported for multispectral processing (Figure S3C). The functional dependency of MSOT signal and Cy7 concentration was determined by phantom study. As shown in Figure S3B, linear correlation between the MSOT signal and Cy7 concentration could be observed. Therefore, the MSOT measurements can provide the relative quantification of the imaging agents *in vivo*.

3.2. In Vivo Pharmacokinetics and Biodistribution of P5Mx Copolymers. In our previous work, we have observed that P5M35 copolymers exhibit rapid clearance feature due to its negative charge. In order to figure out whether the blood clearance and biodistribution pattern of P5Mx copolymers is molecular weight dependent, the pharmacokinetics and biodistribution of P5Mx copolymers with different MAGG content were investigated. Figure 2 illustrates the blood clearance (A) and biodistribution (C) of P5Mx copolymers. Similar clearance rate could be found for copolymers with different MAGG content. This result indicates that for copolymers with excess negative charge, the negative charge play the dominant role in the clearance of copolymers despite their different molecular weight. The biodistribution histograms revealed that the negatively charged copolymers mainly accumulated in liver after injection which is in accordance

with our previous report.²⁰ According to the literature, this might be due to the polyanionic scavenger receptors on macrophage-like cells or endothelial cells in the RES organs, which leads to the extremely low plasma concentration of polymers.^{34,35}

Despite the different molecular weight of P5M20, P5M40, P5M60, and P5M80, their biodistribution patterns showed no obvious difference, as shown in Figure 2B. The difference lies in the liver accumulation level. The radio signal of P5M20 in liver is lower than P5M80 at the early stage (0.5 h), while it reaches almost equal level at 1 h. This could be explained by relatively longer PMAGG block length for P5M80, which may facilitate the RES uptake.

It is well-known that the renal excretion threshold is about 4–5 nm,³⁶ that is about 40000–50000 Da for PHPMA copolymers.³⁷ Therefore, copolymers with molecular weight less than 40000 are easily excreted by glomerular filtration. On the other hand, the linear structure of the above-mentioned PEG-*b*-PMAGG copolymers may facilitate the passing of copolymers through the pore structure in kidney.^{38,39} Therefore, it is reasonable to observe radioactive signals in the bladder region of all P5Mx treated mice. Due to the nondegradable feature of the block copolymers, they are hard to be degraded by enzymes in liver tissue. Therefore, liver continuously exhibit high radioactive signals, the final concentration still remains at about 10 ID% / g for all copolymers at 48 h post-injection (p.i.).

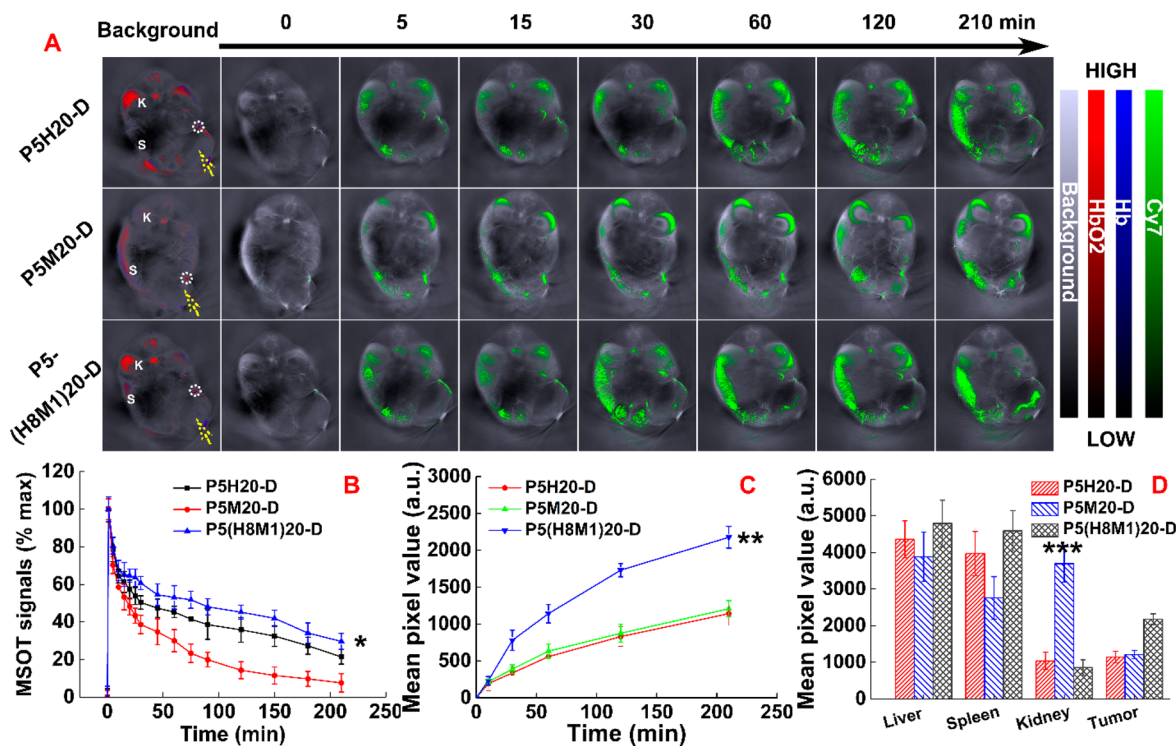


Figure 3. (A) Representative *in vivo* photoacoustic image of 4T1 tumor (marked as yellow arrow) bearing BALB/c mice treated with polymer conjugates P5H20-D, P5M20-D, and P5(H8M1)20-D during 210 min p.i. The images were acquired at the spleen (S), kidney (K), and tumor cross section. (B) Plot of the MSOT signals (converted from the mean Cy7 signal value inside the ROI as marked by white circle, the results were presented as the percentage of the maximum intensity) in blood vs time in 210 min p.i. (* $P < 0.05$ for the blood clearance of P5(H8M1)20-D vs P5M20-D). (C) Mean pixel values of Cy7 in tumor vs time (** $P < 0.005$ for the tumor accumulation of P5(H8M1)20-D vs P5M20-D or P5H20-D). (D) Mean pixel values of Cy7 in liver, spleen, kidney, and tumor region at 210 min p.i. The initial PA signal intensities of the conjugates were maintained as the same (*** $P < 0.005$ for the kidney accumulation of P5M20-D vs P5H20-D and P5(H8M1)20-D).

The above results inspired us that, during the design of the drug delivery system, an excess amount of negative charge should be avoided so as to reduce the RES uptake.

3.3. In Vivo Biodistribution Study of P5(HyMz)m-D Conjugate Micelles. Our previous work has proved that the introduction of HPMA into the PMAGG block can significantly improve their blood circulation and biodistribution. However, those findings were accomplished based on copolymers without drug loadings. It is predictable that, when the anticancer drugs were introduced into the polymer chains, the solution behavior of the final polymer–drug conjugates will undergo drastic change. This has been proved by the increase of hydrodynamic size and alteration of zeta potential in Figure 1 and Table 2.

Various imaging techniques can be used to investigate the biodistribution of polymer–drug conjugate noninvasively. In this work, to avoid the undesired denaturizing of loaded drug or the acid-labile linker, water-soluble alkyne functionalized NIR dye Cy7 was linked to the polymer backbone via a copper-mediated “click chemistry” in a relatively mild reaction condition. As-prepared fluorescent micelles were then subjected to the *in vivo* photoacoustic and fluorescent imaging.

To reveal the influence of negative charge on the plasma circulation and biodistribution of the micelles, 4T1 tumor bearing mice were treated with P5H20-D, P5M20-D, and P5(H8M1)20-D, respectively. Figure 3A illustrates the distribution of these conjugates in spleen, kidney, and tumor during 210 min p.i. The corresponding distribution of conjugates in liver could be found in Figure S4. The plasma concentration change versus time for these conjugates was calculated by the mean pixel values in the ROI (white circle)

and showed as the percentage of the maximum value, as shown in Figure 3B.

Unsurprisingly, P5M20-D exhibited the fastest clearance rate among the tested conjugates due to the excess negative charge. However, it is different from the distribution patterns of the PSMx copolymers without drug loadings, which showed only high liver accumulation. Low deposition in liver and spleen while high kidney accumulation could be found for P5M20-D. The change of the distribution pattern of P5M20-D compared with P5M20 may be caused by the alteration of the solution properties of P5M20-D after the conjugation of anticancer drug. Part of the MAGG group flipped inside the aggregates with partially hydrophobic Dox so that less negative charge appeared on the hydrophilic corona. The rest of MAGG group on the hydrophilic part will cooperate with PEG to avoid the excessive RES uptake and prolong the circulation life of conjugate.

More detailed locally enlarged view of the kidney region could be found in Figure S5. The suborgan distribution showed that the signal of P5M20-D mainly restricted in the cortex region of kidney. On the contrary, distribution of conjugates at both cortex and medulla region could be found for P5H20-D and P5(H8M1)20-D. According to the literature, the three-layered barrier inside glomerulus consists of the fenestrated endothelium, podocyte foot processes with bridging slit diaphragms, and the intervening glomerular basement membrane.⁴⁰ Negative charge is associated with each of the three layers and is thought to retard filtration of anionic molecules, such as albumin, facilitate filtration of cationic molecules and have little impact on neutral molecules,^{40–42} wherefore,

PSM20-D with negative charge is hard to be excreted through renal filtration. More detailed characterization about the kidney distribution is needed because the charge selectivity theory still remain controversial.

Figure 3C showed the time related tumor accumulation of various conjugates during the initial 210 min p.i. Figure 3D illustrated the organ distribution of conjugates at 210 min p.i. From these results it can be found that the longer circulatory half-life for P5(H8M1)20-D caused by the introduction of moderate amount of negative charge has led to higher tumor accumulation. However, the liver and spleen uptake for PSH20-D and P5(H8M1)20-D is higher than that of PSM20-D. This can also be explained by the less negative charge and larger size caused by the inversion of the partially hydrophobic Dox, which made these conjugates susceptible to RES uptake.

Figure 4A represents the photoacoustic imaging results of PSH20-D, PSM20-D, and P5(H8M1)20-D at 24 h p.i., from

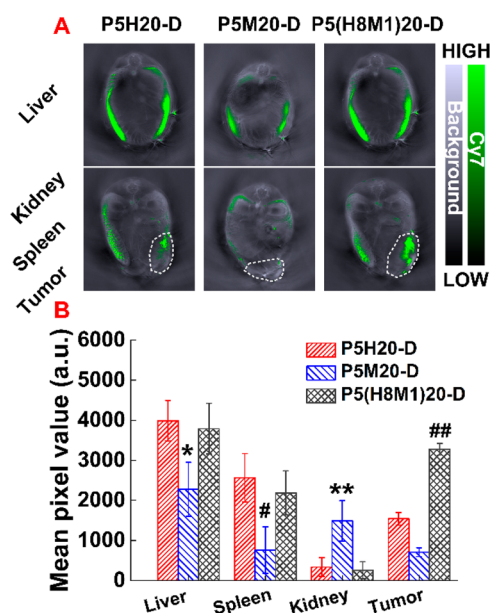


Figure 4. (A) Representative in vivo photoacoustic image of 4T1 tumor (marked as white dashed line) bearing BALB/c mice treated with polymer conjugates PSH20-D, PSM20-D, and P5(H8M1)20-D at 24 h p.i. (B) Mean pixel values of Cy7 in liver, spleen, kidney, and tumor region at 210 min p.i. (*P < 0.05 for the liver uptake of PSM20-D vs PSH20-D and P5(H8M1)20-D; **P < 0.05 for the kidney accumulation of PSM20-D vs PSH20-D and P5(H8M1)20-D; #P < 0.05 for the spleen uptake of PSM20-D vs PSH20-D and P5(H8M1)20-D; ##P < 0.005 for the tumor accumulation of P5(H8M1)20-D vs PSH20-D and PSM20-D).

which almost no PA signal could be observed in blood for all conjugates. The corresponding quantification of organ distribution was displayed in Figure 4B. PSM20-D showed low accumulation in all organs except kidney in which its accumulation was the highest among three conjugates. In contrast, P5(H8M1)20-D and PSH20-D showed higher tumor uptake than PSM20-D. Moreover, P5(H8M1)20-D showed higher tumor accumulation than PSH20-D, while their liver and spleen uptake maintained at the same level. This is mainly because of the longer circulatory half-life of P5(H8M1)20-D, which brought more opportunities for the conjugates to enter the interior of tumor tissue.

To evaluate the potential of enhancing the tumor accumulation by increasing the molecular weight of polymer conjugates. P5(H8M1)80-D with higher molecular weight was synthesized and subjected to in vivo living imaging analysis. Figure 5 represents the in vivo fluorescent image of BALB/c mice bearing subcutaneous 4T1 tumor (marked as yellow arrow) treated with free Cy7 and polymer conjugates PSH20-D, PSM20-D, P5(H8M1)20-D, and P5(H8M1)80-D. All images were intensity weighted and displayed as hot color profile. More detailed images of three paralleled mice in each group can be found in Figure S6.

It can be found from Figure 5 that the organ distribution of various conjugates showed much the similar pattern as the photoacoustic results. The slight difference of the organ distribution was mainly due to the different penetrating ability of light and ultrasonic wave. The fluorescent signal of free Cy7 decreased fast and vanished in 24 h p.i. Almost no fluorescent signal could be detected during further experimental time, that is, 48 and 72 h. However, strong fluorescence in whole body could be observed at 24 h for all micelles. Even for longer experimental time, the fluorescent signal can still be detected. This indicated that micelles possess longer circulation time than free Cy7. Obvious tumor accumulation could only be observed for P5(H8M1)80-D, indicating the enhanced passive targeting ability of the conjugates with high molecular weight. Besides, fluorescent signals could also be found in bladder region for all micelles even if their molecular weight is higher than renal threshold. This indicated that the conjugates are excretable. According to the literature, a flexible, loosely coiled polymer could readily deform to pass through a pore.⁴³ Therefore, all polymer conjugates in this work can be excreted by renal filtration, and the only difference lies in the renal filtration velocity of conjugates with different molecular weights and different amounts of negative charge.

To explore more detailed organ distribution, all mice were anesthetized and sacrificed at 72 h after injection. The ex vivo images showed that free Cy7 was completely eliminated. For PSH20-D and P5(H8M1)20-D, only weak residual fluorescence in main organs such as liver, lung, and kidney could be found. For PSM20-D, the fluorescent signals in liver and spleen were similar to its less negatively charged counterparts, but the signals in kidney were much higher. In contrast, strong fluorescence could be observed in liver and spleen for P5(H8M1)80-D, indicating the elevated RES uptake. The stronger fluorescent signals in kidney for P5(H8M1)80-D than PSH20-D and P5(H8M1)20-D might be mainly caused by the size selectivity of kidney filtration.

Above all, we have proved that the introduction of longer PEG block and moderate amount of negative charge (~10%) can prolong the circulation time and reduce nonspecific organ uptake. In the meantime, longer circulation time and higher tumor accumulation can also be achieved by the increase of molecular weight of PHPMA copolymer, which slows down the renal excretion. It is reasonable to believe that by the rational application of negative charge and molecular weight in the design of nanoscaled carrier system, more optimized delivery system with resistance to nonspecific organ uptake and glomerular filtration could be obtained. In addition, it is noteworthy that PSM20-D with excess negative charge on the drug loading block other than PEG block can specifically accumulated in kidney. Even though the distribution at the cellular level of micelles in kidneys is still not clear. More detailed characterization covering the distribution of the

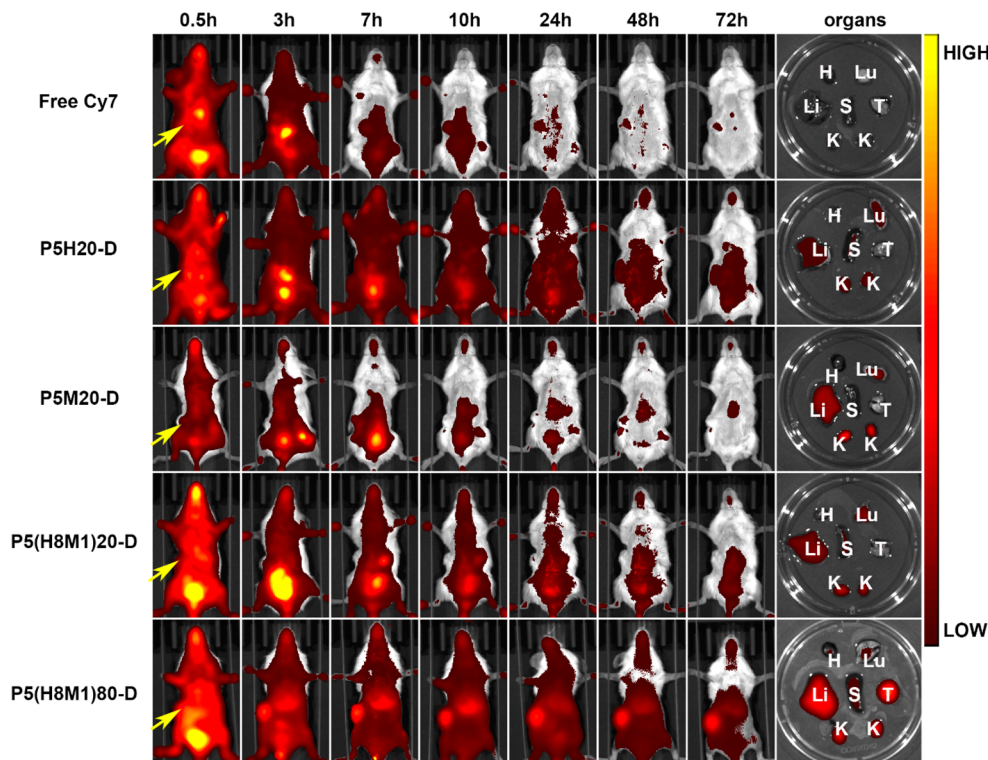


Figure 5. In vivo and ex vivo image of BALB/c mice bearing 4T1 tumor (marked as yellow arrow) treated with free Cy7, polymer conjugates PSH20-D, PSM20-D, P5(H8M1)20-D, and P5(H8M1)80-D at multiple time points p.i.

conjugates in liver and kidney are currently being carried out in our laboratory. However, by now, we still hope that this property may bring an alternative way of treating kidney related cancers such as renal cell carcinoma (RCC).

4. CONCLUSIONS

In this work, a series of well-defined PEG-*b*-PMAGG copolymers with different MAGG content and PEG-*b*-P(HPMA-*co*-MAGG-*co*-HMAGG-*co*-AzMA)-Dox-Cy7 conjugates with different compositions were successfully synthesized via RAFT polymerization and postpolymerization modification technique. The blood circulation, biodistribution, and tumor accumulation were investigated by γ -imaging, in vivo living imaging, and photoacoustic tomography. PEG-*b*-PMAGG copolymers were found to be rapidly cleared out from blood circulation and accumulate in liver despite the different molecular weight of PMAGG block. After the conjugation of anticancer drug, the solution behavior of polymer conjugates underwent noticeable change with part of the carboxyl group flipped inside the formed micelles; thus, longer circulation time and lower liver uptake were achieved. By the appropriate decrease of negative charge and the increase of the molecular weight, the polymer-drug conjugates with lower nonspecific uptake and enhanced tumor accumulation could be obtained. The kidney accumulation of PSM20-D inspired us that the rational application of negative charge may play an active role in slowing down the renal excretion. Beyond this, its kidney specific accumulation also offered us a potential option for treating the kidney related cancer such as renal cell carcinoma (RCC).

ASSOCIATED CONTENT

Supporting Information

The protonated NMR characterization of the polymer conjugates, the physicochemical characterization of the polymer conjugates, the representative in vivo photoacoustic image in liver cross section of tumor bearing BALB/c mice treated with polymer conjugates PSH20-D, PSM20-D, and P5(H8M1)20-D during 210 min p.i., and the detailed in vivo living fluorescent image of three paralleled mice treated with polymer conjugates PSH20-D, PSM20-D, P5(H8M1)20-D, and P5(H8M1)80-D at multiple time point p.i. The Supporting Information is available free of charge on the [ACS Publications website](http://acspublications.org) at DOI: [10.1021/acs.biomac.5b00460](https://doi.org/10.1021/acs.biomac.5b00460).

AUTHOR INFORMATION

Corresponding Author

*Tel. and Fax: +86-10-64432762. E-mail: zhgan@mail.buct.edu.cn.

Author Contributions

[†]These authors contributed equally to this work (Q.Y. and Z.W.).

Notes

The authors declare no competing financial interest.

ACKNOWLEDGMENTS

This work was supported by the National Natural Science Foundations of China (Grant Nos. 51390481, 51025314, 50873109, 81472412, and 30930030) and China Postdoctoral Foundation (Grant No. 2015MS570919). This work was also supported by the long-term subsidy mechanism from the Ministry of Finance and the Ministry of Education of PRC for BUCT.

■ REFERENCES

- (1) Oerlemans, C.; Bult, W.; Bos, M.; Storm, G.; Nijzen, J. F. W.; Hennink, W. E. Polymeric Micelles in Anticancer Therapy: Targeting, Imaging and Triggered Release. *Pharm. Res.* **2010**, *27* (12), 2569–2589.
- (2) Duncan, R. The dawning era of polymer therapeutics. *Nat. Rev. Drug Discovery* **2003**, *2* (5), 347–60.
- (3) Larson, N.; Ghandehari, H. Polymeric conjugates for drug delivery. *Chem. Mater.* **2012**, *24* (5), 840–853.
- (4) Elsabahy, M.; Wooley, K. L. Design of polymeric nanoparticles for biomedical delivery applications. *Chem. Soc. Rev.* **2012**, *41* (7), 2545–2561.
- (5) Peer, D.; Karp, J. M.; Hong, S.; Farokhzad, O. C.; Margalit, R.; Langer, R. Nanocarriers as an emerging platform for cancer therapy. *Nat. Nanotechnol.* **2007**, *2* (12), 751–760.
- (6) Maeda, H. The enhanced permeability and retention (EPR) effect in tumor vasculature: The key role of tumor-selective macromolecular drug targeting. *Adv. Enzyme Regul.* **2001**, *41*, 189–207.
- (7) Matsumura, Y.; Maeda, H. A New Concept for Macromolecular Therapeutics in Cancer-Chemotherapy - Mechanism of Tumoritropic Accumulation of Proteins and the Antitumor Agent Smancs. *Cancer Res.* **1986**, *46* (12), 6387–6392.
- (8) Jokerst, J. V.; Lobovkina, T.; Zare, R. N.; Gambhir, S. S. Nanoparticle PEGylation for imaging and therapy. *Nanomedicine* **2011**, *6* (4), 715–728.
- (9) Veronese, F. M.; Schiavon, O.; Pasut, G.; Mendichi, R.; Andersson, L.; Tsirk, A.; Ford, J.; Wu, G.; Kneller, S.; Davies, J.; Duncan, R. PEG–Doxorubicin Conjugates: Influence of Polymer Structure on Drug Release, in Vitro Cytotoxicity, Biodistribution, and Antitumor Activity. *Bioconjugate Chem.* **2005**, *16* (4), 775–784.
- (10) Duncan, R.; Kopecek, J. Soluble Synthetic-Polymers as Potential-Drug Carriers. *Adv. Polym. Sci.* **1984**, *57*, 51–101.
- (11) Duncan, R.; Hume, I. C.; Kopeckova, P.; Ulbrich, K.; Strohalm, J.; Kopecek, J. Anticancer Agents Coupled to N-(2-Hydroxypropyl)-Methacrylamide Copolymers 0.3. Evaluation of Adriamycin Conjugates against Mouse Leukemia-L1210 Invivo. *J. Controlled Release* **1989**, *10* (1), 51–63.
- (12) Borgman, M. P.; Coleman, T.; Kolhatkar, R. B.; Geyser-Stoops, S.; Line, B. R.; Ghandehari, H. Tumor-targeted HPMA copolymer-(RGDFK)-(CHX-A "-DTPA) conjugates show increased kidney accumulation. *J. Controlled Release* **2008**, *132* (3), 193–199.
- (13) Greenwald, R. B.; Choe, Y. H.; McGuire, J.; Conover, C. D. Effective drug delivery by PEGylated drug conjugates. *Adv. Drug Delivery Rev.* **2003**, *55* (2), 217–250.
- (14) Tucker, B. S.; Sumerlin, B. S. Poly(N-(2-hydroxypropyl)methacrylamide)-based nanotherapeutics. *Polym. Chem.* **2014**, *5* (5), 1566–1572.
- (15) Talelli, M.; Rijcken, C. J.; van Nostrum, C. F.; Storm, G.; Hennink, W. E. Micelles based on HPMA copolymers. *Adv. Drug Delivery Rev.* **2010**, *62* (2), 231–9.
- (16) Lammers, T.; Subr, V.; Ulbrich, K.; Hennink, W. E.; Storm, G.; Kiessling, F. Polymeric nanomedicines for image-guided drug delivery and tumor-targeted combination therapy. *Nano Today* **2010**, *5* (3), 197–212.
- (17) Lammers, T.; Kuhnlein, R.; Kissel, M.; Subr, V.; Etrych, T.; Pola, R.; Pechar, M.; Ulbrich, K.; Storm, G.; Huber, P.; Peschke, P. Effect of physicochemical modification on the biodistribution and tumor accumulation of HPMA copolymers. *J. Controlled Release* **2005**, *110* (1), 103–118.
- (18) Allmeroth, M.; Moderegger, D.; Gundel, D.; Buchholz, H. G.; Mohr, N.; Koynov, K.; Rosch, F.; Thews, O.; Zentel, R. PEGylation of HPMA-based block copolymers enhances tumor accumulation in vivo: A quantitative study using radiolabeling and positron emission tomography. *J. Controlled Release* **2013**, *172* (1), 77–85.
- (19) Wang, D. Q.; Liu, R. G.; Che, N.; Li, Q. M.; Li, Z.; Tian, Y.; Kang, H. L.; Jia, B.; Huang, Y. Improving the blood clearance time of I-125 labeled Dex-g-PMAGGCONHTyr by copolymerization. *Polym. Chem.* **2011**, *2* (8), 1872–1878.
- (20) Yu, Q. S.; Dong, C. Y.; Zhang, J. J.; Shi, J. Y.; Jia, B.; Wang, F.; Gan, Z. H. Synthesis of poly(ethylene glycol)-b-poly(N-(2-hydroxypropyl) methacrylamide) block copolymers with well-defined structures and their influence on in vivo circulation and biodistribution. *Polym. Chem.* **2014**, *5* (19), 5617–5627.
- (21) Brooks, D. J. Positron emission tomography and single-photon emission computed tomography in central nervous system drug development. *NeuroRx* **2005**, *2* (2), 226–36.
- (22) Ntziachristos, V.; Ripoll, J.; Wang, L. H. V.; Weissleder, R. Looking and listening to light: the evolution of whole-body photonic imaging. *Nat. Biotechnol.* **2005**, *23* (3), 313–320.
- (23) Ale, A.; Ermolayev, V.; Herzog, E.; Cohrs, C.; de Angelis, M. H.; Ntziachristos, V. FMT-XCT: in vivo animal studies with hybrid fluorescence molecular tomography-X-ray computed tomography. *Nat. Methods* **2012**, *9* (6), 615–20.
- (24) Kruger, R. A.; Kiser, W. L.; Reinecke, D. R.; Kruger, G. A.; Miller, K. D. Thermoacoustic molecular imaging of small animals. *Mol. Imaging* **2003**, *2* (2), 113–23.
- (25) Wang, X.; Pang, Y.; Ku, G.; Xie, X.; Stoica, G.; Wang, L. V. Noninvasive laser-induced photoacoustic tomography for structural and functional in vivo imaging of the brain. *Nat. Biotechnol.* **2003**, *21* (7), 803–6.
- (26) Fuchs, A. V.; Gemmill, A. C.; Thurecht, K. J. Utilising polymers to understand diseases: advanced molecular imaging agents. *Polym. Chem.* **2015**, *6* (6), 868–880.
- (27) Mitsukami, Y.; Donovan, M. S.; Lowe, A. B.; McCormick, C. L. Water-soluble polymers. 81. Direct synthesis of hydrophilic styrenic-based homopolymers and block copolymers in aqueous solution via RAFT. *Macromolecules* **2001**, *34* (7), 2248–2256.
- (28) Shi, L. J.; Chapman, T. M.; Beckman, E. J. Poly(ethylene glycol)-block-poly(N-vinylformamide) copolymers synthesized by the RAFT methodology. *Macromolecules* **2003**, *36* (7), 2563–2567.
- (29) Rejmanova, P.; Labsky, J.; Kopecek, J. Aminolyses of Monomeric and Polymeric 4-Nitrophenyl Esters of N-Methacryloyl-Amino Acids. *Makromol. Chem.* **1977**, *178* (8), 2159–2168.
- (30) Yu, Q. S.; Zhang, J. J.; Zhang, G.; Gan, Z. H. Synthesis and Functions of Well-defined Polymer-drug Conjugates as Efficient Nanocarriers for Intravesical Chemotherapy of Bladder Cancer(a). *Macromol. Biosci.* **2015**, *15* (4), 509–520.
- (31) Ebbesen, M. F.; Schaffert, D. H.; Crowley, M. L.; Oupicky, D.; Howard, K. A. Synthesis of Click-Reactive HPMA Copolymers Using RAFT Polymerization for Drug Delivery Applications. *J. Polym. Sci., Part A: Polym. Chem.* **2013**, *51* (23), 5091–5099.
- (32) Song, W. T.; Tang, Z. H.; Zhang, D. W.; Burton, N.; Driessens, W.; Chen, X. S. Comprehensive studies of pharmacokinetics and biodistribution of indocyanine green and liposomal indocyanine green by multispectral optoacoustic tomography. *RSC Adv.* **2015**, *5* (5), 3807–3813.
- (33) Wang, J.; Xie, Y. D.; Wang, L. M.; Tang, J. L.; Li, J. Y.; Kocae, D.; Kocae, Y.; Zhang, Z. W.; Li, Y. P.; Chen, C. Y. In vivo pharmacokinetic features and biodistribution of star and rod shaped gold nanoparticles by multispectral optoacoustic tomography. *RSC Adv.* **2015**, *5* (10), 7529–7538.
- (34) Platt, N.; Gordon, S. Is the class A macrophage scavenger receptor (SR-A) multifunctional? - The mouse's tale. *J. Clin. Invest.* **2001**, *108* (5), 649–654.
- (35) Bijsterbosch, M. K.; Manoharan, M.; Rump, E. T.; De Vreue, R. L.; van Veghel, R.; Tivel, K. L.; Biessen, E. A.; Bennett, C. F.; Cook, P. D.; van Berkel, T. J. In vivo fate of phosphorothioate antisense oligodeoxynucleotides: predominant uptake by scavenger receptors on endothelial liver cells. *Nucleic Acids Res.* **1997**, *25* (16), 3290–6.
- (36) Venkatachalam, M. A.; Rennke, H. G. The structural and molecular basis of glomerular filtration. *Circ. Res.* **1978**, *43* (3), 337–47.
- (37) Seymour, L. W.; Duncan, R.; Strohalm, J.; Kopecek, J. Effect of Molecular-Weight (Mw) of N-(2-Hydroxypropyl)Methacrylamide Copolymers on Body Distribution and Rate of Excretion after Subcutaneous, Intraperitoneal, and Intravenous Administration to Rats. *J. Biomed. Mater. Res.* **1987**, *21* (11), 1341–1358.

- (38) Etrych, T.; Subr, V.; Strohalm, J.; Sirova, M.; Rihova, B.; Ulbrich, K. HPMA copolymer-doxorubicin conjugates: The effects of molecular weight and architecture on biodistribution and in vivo activity. *J. Controlled Release* **2012**, *164* (3), 346–354.
- (39) Chytil, P.; Hoffmann, S.; Schindler, L.; Kostka, L.; Ulbrich, K.; Caysa, H.; Mueller, T.; Mader, K.; Etrych, T. Dual fluorescent HPMA copolymers for passive tumor targeting with pH- sensitive drug release II: Impact of release rate on biodistribution. *J. Controlled Release* **2013**, *172* (2), 504–512.
- (40) Miner, J. H. Glomerular filtration: the charge debate charges ahead. *Kidney Int.* **2008**, *74* (3), 259–261.
- (41) Rennke, H. G.; Patel, Y.; Venkatachalam, M. A. Glomerular filtration of proteins: clearance of anionic, neutral, and cationic horseradish peroxidase in the rat. *Kidney Int.* **1978**, *13* (4), 278–288.
- (42) Rennke, H. G.; Cotran, R. S.; Venkatachalam, M. A. Role of molecular charge in glomerular permeability. Tracer studies with cationized ferritins. *J. Cell Biol.* **1975**, *67* (3), 638–646.
- (43) Fox, M. E.; Szoka, F. C.; Frechet, J. M. J. Soluble Polymer Carriers for the Treatment of Cancer: The Importance of Molecular Architecture. *Acc. Chem. Res.* **2009**, *42* (8), 1141–1151.